Key Points:

- Sixteen relevant tidal lines identified in hourly data from ERA5 atmospheric reanalysis
- Dedicated simulations with a high-resolution global hydrodynamic model to simulate ocean tides with atmospheric influence
- New tidal models reduce pre-fit residuals in GRACE-FO Laser Ranging Interferometer data

Correspondence to:

K. Balidakis,
kyriakos.balidakis@gfz-potsdam.de

Atmospheric Contributions to Global Ocean Tides for Satellite Gravimetry

Kyriakos Balidakis[1] , Roman Sulzbach[1,2] , Linus Shihora[1] , Christoph Dahle[1] , Robert Dill[1] , and Henryk Dobslaw[1]

[1]Department 1: Geodesy, GFZ German Research Centre for Geosciences, Potsdam, Germany, [2]Institut für Meteorologie, Freie Universität Berlin, Berlin, Germany

Abstract To mitigate temporal aliasing effects in monthly mean global gravity fields from the GRACE and GRACE-FO satellite tandem missions, both tidal and non-tidal background models describing high-frequency mass variability in atmosphere and oceans are needed. To quantify tides in the atmosphere, we exploit the higher spatial (31 km) and temporal (1 hr) resolution provided by the latest atmospheric ECMWF reanalysis, ERA5. The oceanic response to atmospheric tides is subsequently modeled with the general ocean circulation model MPIOM (in a recently revised TP10L40 configuration that includes the feedback of self-attraction and loading to the momentum equations and has an improved bathymetry around Antarctica) as well as the shallow water model TiME (employing a much higher spatial resolution and more elaborate tidal dissipation than MPIOM). Both ocean models consider jointly the effects of atmospheric pressure variations and surface wind stress. We present the characteristics of 16 waves beating at frequencies in the 1–6 cpd band and find that TiME typically outperforms the corresponding results from MPIOM and also FES2014b as measured from comparisons with tide gauge data. Moreover, we note improvements in GRACE-FO laser ranging interferometer range-acceleration pre-fit residuals when employing the ocean tide solutions from TiME, in particular, for the S_1 spectral line with most notable improvements around Australia, India, and the northern part of South America.

Plain Language Summary In addition to many rather slow processes such as the melting of glaciers, rapid mass redistribution related to the weather also measurably affect the Earth's gravity field. The ability of monitoring liquid freshwater changes within the Earth system from the satellite gravity missions GRACE (2002–2017) and GRACE-FO (since 2018) relies on accurate background models of mass variability in atmosphere and oceans for both tidal and non-tidal processes. Atmospheric tides are primarily excited in the middle atmosphere by solar energy absorption at periods of 24 hr and its overtones. We find additional tidal signatures in the atmosphere excited by periodic deformations of both crust and sea-surface of the Earth. We thus introduce here a new data set for the atmospheric tides and their corresponding oceanic response that features both more waves and higher accuracy than other background models previously used for the processing of GRACE and GRACE-FO satellite gravimetry data.

1. Introduction

Periodic mass transport oscillations across a wide range of frequencies are not only observed in the oceans but also in the atmosphere where they constitute a substantial part of the sub-diurnal variability particularly in the tropics (Ray & Ponte, 2003). The physical mechanisms governing atmospheric tides have been extensively studied for many years already (Chapman & Lindzen, 1970; Dieminger et al., 1996; Lindzen & Chapman, 1969). Tides are predominantly excited by water vapor periodically absorbing infrared radiation and ozone absorbing ultraviolet radiation. Changes in temperature and thus density in primary excitation regions of the (tropical) middle atmosphere emanate both vertically and horizontally and thus affect the atmospheric state quantities at levels as high as the thermosphere (Teitelbaum & Vial, 1981) and also down at the surface, where notable variations in both atmospheric pressure and the associated surface winds have been recorded (Ray, 1998a).

Periodic pressure changes recorded by in situ barometers can also be manifestations of periodic height changes of the lower atmospheric boundary layer stemming from both solid Earth and ocean tides. Such variations are primarily induced by the tide-raising lunisolar gravitational potential. This forcing mechanism has been found to be particularly effective for the principal semi-diurnal lunar tide M_2, where excitations in the middle atmosphere

are basically non-existent (Vial & Forbes, 1994). Even though the temporally varying height of Earth's crust and the sea surface are not considered in numerical weather prediction models, signatures of this tide have been found to be quite accurately represented in data from the European Centre for Medium-Range Weather Forecasts (ECMWF) due to the comparatively high weight of data from dense barometer networks in the ECMWF data assimilation system (Schindelegger & Dobslaw, 2016).

With the recent availability of ECMWF's latest reanalysis, ERA5 (Hersbach et al., 2020), which features an increased temporal resolution (hourly resolution as opposed to three-hourly or even six-hourly sampling from previously available data sets), we aim at reassessing the representation of atmospheric tides in a state-of-the-art global atmospheric data set. In addition, we reassess the oceanic response to atmospheric tides with dedicated numerical simulations with both the ocean general circulation model MPIOM (Jungclaus et al., 2013) and the high-resolution barotropic model TiME (Sulzbach et al., 2021) that is employing the shallow water equations. Employing hourly sampling makes special temporal interpolation schemes (Ponte & Ray, 2002; van den Dool et al., 1997) superfluous and thus eliminates the associated artifacts.

Accurate models of global atmospheric tides and their oceanic response are in particular important for the processing of satellite gravimetry data as collected by GRACE (Tapley et al., 2004) and GRACE-FO (Landerer et al., 2020). Those missions utilize precise ranging between two spacecraft trailing each other in a polar orbit at altitudes below 500 km. Sensor data are typically accumulated over 30 day intervals for the calculation of a single monthly mean gravity field that is indicative of large-scale ice and water mass changes over the continents when compared to gravity fields obtained at other epochs in time. Mass variations at periods shorter than twice the accumulation period need to be corrected by background models originating from independent data in order to avoid temporal aliasing (Tierney et al., 2000). Background models as the Atmosphere and Ocean De-Aliasing Level-1B (AOD1B) product simulate the effects of non-tidal circulation in the atmosphere and the oceans on Earth's gravity field by employing high-resolution numerical weather models fields, and are routinely applied at the observation equation level in the GRACE/GRACE-FO data processing scheme (Dobslaw et al., 2017; Shihora et al., 2022). Thorough assessments of the overall mission performance of GRACE and GRACE-FO (Flechtner et al., 2015) revealed that errors in tidal background models are among the top-three sources of noise and artefacts in the monthly gravity fields. Thus, these errors are one of the reasons why the baseline accuracy anticipated prior to the launch of GRACE (Kim et al., 2001) is still not reached by the latest releases of monthly mean gravity fields. Continued efforts to improve the time-variable background models are therefore of critical importance for the overall accuracy of the mission's primary science data products.

In this contribution, we reassess periodic mass variations in the atmosphere in the diurnal regime and higher frequencies. The analysis will be based on 8 years of hourly pressure data from ERA5 and a corresponding MPIOM simulation as introduced in Section 2. In Section 3, the methodology for the isolation of tidal signatures from the atmospheric forcing fields (pressure and wind stress) is outlined, followed by a discussion of tidal signatures found in the transient series of atmospheric surface and ocean bottom pressure (Section 4). Subsequently, we simulate the ocean bottom pressure response at all 16 frequencies with the high-resolution global ocean tide model TiME (Sulzbach et al., 2021), and study in more detail the individual contributions of various forcing agents to the total ocean tide at the S_1 frequency (Section 5). The article concludes with a first application of the new tide models from ERA5 and TiME in GRACE-FO data processing (Section 6) followed by a brief summary (Section 7).

2. Transient Time-Series From ERA5 and MPIOM

ECMWF's latest global atmospheric reanalysis, ERA5 (Hersbach et al., 2020), succeeded ERA-Interim (Dee et al., 2011) and features several improvements including the enhanced spatio-temporal resolution (analysis hourly on TL639 grids on 137 hybrid sigma-pressure levels in lieu of 6-hourly on TL255 grids on 60 model levels) and the more advanced version of the integrated forecasting system (c41r2 is 10 years ahead of c31r2). ERA5 has proven to be on average more accurate than other state-of-the-art atmospheric reanalysis including NASA's MERRA2 (Gelaro et al., 2017) and the Japanese JRA55 (Kobayashi et al., 2015), mostly owing to its high spatial resolution, the more recent data assimilation scheme, and the volume of observations it assimilates. Taszarek et al. (2021) found that ERA5 shows higher correlation as well as lower mean absolute errors with respect to MERRA2, in terms of comparing an ensemble of 45 convective variables including moisture, wind, and temperature with in situ observations over Europe and North America. Hassler and Lauer (2021) report that

in comparison to in situ gauges, ERA5 has smaller precipitation biases, on average, when compared to MERRA2 and JRA55. Huang et al. (2021) found that GNSS-derived precipitable water vapor, which is an important measure of moisture in the atmosphere, over the Tibetan Plateau has a better agreement to ERA5 in comparison to MERRA2, especially in terms of high-frequency variations. Malakar et al. (2020) found that ERA5 better represents the structure of tropical cyclones compared to other models including MERRA2 and JRA55, as well as ERA-Interim, GFS (Sela, 2010), and CFSv2 (Saha et al., 2014). In addition to surface pressure fields at the reference orography, 3D temperature and specific humidity fields are required to build pressure fields at the orography employed for AOD1B RL07 (Shihora et al., 2022), following the procedure described in Dobslaw (2016). Moreover, to force general ocean circulation models such as MPIOM, other fields are necessary in addition to surface pressure, namely, the instantaneous turbulent surface (wind) stress, 10 m wind speed, temperature as well as dew point temperature at 2 m above the orography, total cloud cover, downward short-wave radiation at the orography, and total precipitation. We note that from all these fields, only harmonic coefficients estimated from pressure and wind stress are utilized to force the TiME simulations. For this study, we use 8 years (2007–2014) of hourly surface pressure fields given at the native grid of ERA5. By design, the selected period corresponds to estimation period applied in Dobslaw et al. (2016) so that the results may be readily compared to these prior estimates based on operational ECMWF analysis and forecast data.

We also make use of a dedicated simulation with the Max-Planck-Institute Global Ocean/Sea-Ice Model MPIOM (Jungclaus et al., 2013), which is a direct descendant of the Hamburg Ocean Primitive Equation Model (HOPE) (Drijfhout et al., 1996; Wolff et al., 1997). MPIOM is a free surface general circulation model that solves the primitive equations under the Boussinesq approximation (Marsland et al., 2003). It uses a horizontal Arakawa-C and a vertical z-grid and features full feedbacks from the effects of self-attraction and loading (SAL) including contributions from surface pressure anomalies over the continents (Shihora et al., 2021). SAL, which has a significant impact both for tidal as well as non-tidal high-frequency variability in the oceans, describes both the feedbacks from the self-attraction of the water column as well as the deformation of the solid Earth caused by anomalous surface loads (e.g., Farrell, 1972; Gordeev et al., 1977; Hendershott, 1972; Ray, 1998b). Additionally, the deformation and attractional effects of anomalous surface pressure loads over the continents can contribute to ocean dynamics, namely in coastal areas (Shihora et al., 2021), so that those are explicitly considered in our study. For a more detailed description of the implementation we refer to Section 5. The experiment applies MPIOM's TP10L40 configuration with a 1° tri-polar grid and 40 vertical layers. The internal time-step is set to 20 min. The model is spun-up for 2,000 years from 3D temperature and salinity climatologies (Levitus et al., 2005) and cyclic atmospheric forcing with daily sampling (Röske, 2005). Following are transient simulations based on the ECMWF's atmospheric ERA5 reanalysis data as hourly forcing, including wind-stress and surface pressure contributions. While no forcing through a lunisolar gravitational potential is applied, atmospheric tides influence the ocean state indirectly via the associated variations in the atmospheric pressure and wind stress forcing fields. Hourly ocean bottom pressure output will be used here again from the years 2007–2014.

3. Selection of Relevant Tidal Lines

For the extraction of periodic signals from a time-series of pressure anomalies at a given place, we assume that the transient variations $y(t)$ are the sum of four different signal groups

$$y = y_p + y_h + y_a + \epsilon. \tag{1}$$

The first addend in Equation 1 denotes long-wavelength variations that may be approximated by a low-degree polynomial, for example, $y_p = \sum_i x_i t^i$ with $i \leq 0$. In our case of working with atmospheric reanalysis data, the polynomial term estimates x_i are largely not statistically significant for $i > 1$ and will not be considered any further. Non-tidal anomalies associated with synoptic weather variations are denoted by y_a and superimposed noise arising either from geophysical sources or random errors is denoted by ϵ. The harmonic variations y_h that are of interest in this paper are described by the following ansatz

$$y_h(t) = \sum_j A_j \cos(\chi_j(t) - \phi_j) = \sum_j C_j \cos(\chi_j(t)) + S_j \sin(\chi_j(t)), \tag{2}$$

where given a certain wave j with a particular frequency, A_j denotes the amplitude, ϕ_j denotes the phase, and C_j and S_j denote the in-phase and quadrature components, respectively. We do not allow for nodal corrections

(e.g., Schureman, 1958) since they are not justified on physical grounds for radiational atmospheric tides and they fail to achieve a significant level of de-modulation for the high-frequency variations of interest. The time-dependent astronomical argument for each wave in Equation 2 is given following Doodson (1921) and Pugh and Woodworth (2014)

$$\chi = q_1 \tau + q_2 s + q_3 h + q_4 p + q_5 N' + q_6 p_s + q_7 \frac{\pi}{2},$$

(3)

where τ is the mean lunar time, s is the mean longitude of the Moon, h is the mean longitude of the Sun, p is the mean longitude of the lunar perigee, N' is the negative of the longitude of the Moon's mean ascending node on the ecliptic, and p_s is the mean longitude of the solar perigee. Doodson's fundamental arguments are calculated following Tamura (1987). The set of seven multipliers q_i uniquely identifies both the speed and equilibrium phase of each wave.

For each grid node, we concurrently estimate C_j and S_j of all waves in a single adjustment in lieu of A_j and φ since the least squares problem is rendered linear, thus eliminating the need to perform iterations on that account. We found that it is slightly better in terms of variance explained by each wave of the ensemble (see Equation 4) to solve for the waves of interest together with other waves at frequencies that span from inter-annual time-scales down to the Nyquist period by employing raw data directly, in lieu of band-pass filtered data as applied by Dobslaw et al. (2017). Given the frequency set-up and the data sets employed, the correlations between the estimated coefficients for the different constituents are not statistically significant. For a discussion over the spatial and temporal correlations of the time series of interest as well as the estimated harmonic estimate amplitudes and the associated Stokes coefficients, the interested reader is referred to Supporting Information S1.

We also test the potential impact of assumptions about spatial and temporal error correlations in the time-varying pressure fields on the least squares estimation process (see Supporting Information S1) and find no significant impact on the results. We thus consider the results presented in the following as numerically robust.

Individual tidal waves in the atmosphere that are to be considered in this article are selected based on the following requirements:

1. Amplitudes should exceed 5 Pa in amplitude, on a global area-weighted average;
2. Phases should be correlated over several hundred kilometers;
3. Amplitudes and phases should be rather similar when estimated from data of different years;
4. The period of each wave must not be longer than a day;
5. The Rayleigh criterion must be fulfilled; (e.g., Godin, 1972) for all considered pairs; and
6. Each wave should lead to a post-fit residual scatter reduction.

For all waves under consideration, we perform F-Tests by evaluating the inequality $\hat{\mathbf{x}}_{\mathbf{j}}^{\mathsf{T}} \mathbf{Q}_{\hat{\mathbf{x}}_{\mathbf{j}}}^{-1} \hat{\mathbf{x}}_{\mathbf{j}} \left(2\hat{\sigma}^2\right)^{-1} \leq F_{2,f}^{\alpha}$, where $\hat{\mathbf{x}}_{\mathbf{j}}$ denotes the harmonic amplitudes of wave j, $\mathbf{Q}_{\hat{\mathbf{x}}_{\mathbf{j}}}$ is the block of the related cofactor matrix, $\hat{\sigma}^2$ is the a posteriori unit variance, and $F_{2,f}^{\alpha} \approx 3.0$ is the F-distribution value for significance level $\alpha = 0.05$ given hourly multi-year time series. Then, we calculate the portion of the signal variance explained by the harmonic estimates of each wave set up

$$\kappa_j = \frac{\sigma_{y(\mathbf{x},t)}^2 - \sigma_{y_h(t,C_j(\mathbf{x}),S_j(\mathbf{x}))}^2}{\sigma_{y(\mathbf{x},t)}^2}$$

(4)

where σ^2 denotes variance, $y(\mathbf{x}, t)$ denotes the time series, and $y_h(t, C_j(\mathbf{x}), S_j(\mathbf{x}))$ denotes the contribution of wave j, which is a function of node-specific ($\mathbf{x}$) harmonic coefficients. Since for no wave at the diurnal and other higher-frequency bands all grid nodes yield a statistically significant decrease in the variance of the post-fit residuals, to facilitate the quantification of the tidal fit's utility in describing high-frequency variations, we calculate global average κ coefficients (see Equation 4) by convolving amplitudes to an area-dependent weighting kernel. Failing to account for the decreasing surface area represented by each grid node as function of $|\varphi|$ (φ: latitude) leads to an erroneously limited wave ensemble since tidal variations in pressure are not prominent in polar and sub-polar regions which are overrepresented in equiangular grids.

Our analysis of ERA5 data leads to changes with respect to the wave list previously employed for AOD1B RL06. In the following, π_1, ψ_1, K_2, S_4, S_5, and S_6 are considered additionally, whereas N_2 and L_2 will be excluded.

Table 1
Extended Doodson (Solar-Day-Based) and Delaunay Argument Multipliers (Hartmann & Wenzel, 1995; Simon, 2013) for 16 Waves of Diurnal and Shorter Periods in Atmosphere and Ocean That Were Found to Be Relevant for Satellite Gravimetry

Darwin name	Frequency (°h^{-1})	Doodson arguments							Delaunay arguments						Argument at J2000 (○)
		τ	s	h	p	N'	p_s	90°	γ	l	l'	F	D	Ω	
π_1	14.91786609	1	1	−3	0	0	1	−1	1	0	1	2	−2	2	171.999
P_1	14.95893277	1	1	−2	0	0	0	−1	1	0	0	2	−2	2	169.528
S_1	15.00000141	1	1	−1	0	0	1	1	1	0	1	0	0	0	192.932
K_1	15.04107005	1	1	0	0	0	0	1	1	0	0	0	0	0	190.461
ψ_1	15.08213673	1	1	1	0	0	−1	1	1	0	−1	0	0	0	187.990
M_2	28.98410705	2	0	0	0	0	0	0	2	0	0	2	0	2	124.288
T_2	29.95893614	2	2	−3	0	0	1	0	2	0	1	2	−2	2	2.459
S_2	30.00000282	2	2	−2	0	0	0	−1	2	0	0	2	−2	2	269.988
R_2	30.04106950	2	2	−1	0	0	−1	2	2	0	−1	2	−2	2	177.517
K_2	30.08214010	2	2	0	0	0	0	0	2	0	0	0	0	0	200.921
T_3	44.95893559	3	3	−4	0	0	0	0	3	0	0	4	−4	4	259.516
S_3	45.00000423	3	3	−3	0	0	0	2	3	0	0	3	−3	3	359.983
R_3	45.04107287	3	3	−2	0	0	0	0	3	0	0	2	−2	2	100.449
S_4	60.00000564	4	4	−4	0	0	0	0	4	0	0	4	−4	4	359.977
S_5	75.00000705	5	5	−5	0	0	0	0	5	0	0	5	−5	5	179.971
S_6	90.00000846	6	6	−6	0	0	0	0	6	0	0	6	−6	6	359.965

The argument multipliers $q_i \in \mathbb{Z}$ are tabulated in Table 1 along with the associated Delaunay fundamental variables (the Greenwich mean sidereal time γ, the mean anomaly of the Moon l, the mean anomaly of the Sun l', the mean elongation of the Moon D, the mean longitude of the lunar node Ω, and $F = s - \Omega$). We note that for the calculation of q_7 which describes the wave phase, we employ the harmonic amplitudes $V_g|c^\omega$ and $V_g|s^\omega$ of the wave-specific gravitational tide-raising potential $\left(q_7 = 2\tan^{-1}(V_g|s^\omega, V_g|c^\omega)\pi^{-1}\right)$. Please note that there are exceptions for other tidal species. These exceptions depend upon degree and order, reading (n, m), of the respective partial tide and apply for long-period tides ([2, 0] and [3, 0]), as well as diurnal third-degree tides (3,1). A detailed formula for tides up to degree-3: $q_7^{n,m} = 2\tan^{-1}(V_g|s^\omega, V_g|c^\omega)\pi^{-1} + 2\delta_{m0}(\delta_{n2} + \delta_{n3}) + 2\delta_{m1}\delta_{n3}$, where $n \in [2, 3]$, $m \in [0, n]$, and δ_{nm} is th Dirac delta function.

It is instructive to transform the resulting grids for in-phase and quadrature phase of each tidal wave into Stokes Coefficients and calculate power spectra (Rapp, 1982) as displayed in Figure 1 (see Section S6 and Equation S4 of Supporting Information S1). Degree variance implicitly expresses the average de-correlation length and therefore the field smoothness and the ability to perform predictions in the spatial domain (e.g., Kaula, 1959), hence illustrates quite nicely the fulfillment of our selection requirements (a) and (b) given above.

For surface pressure from ERA5 (see Figure 1a), a dominant degree 2 pattern is evident for the S_2 tidal wave. At other spatial scales, the signals at the S_1 frequency are dominant, which is not surprising in view of the diurnal variation of solar irradiation which primarily drives all atmospheric tide signals. It is interesting to note that for waves with beat frequencies around 3–6 cpd, S_3 has still the most energy but it is closely followed by its side lines T_3 and R_3 (T_3, S_3, and R_3 differ by only 1 cpy). All other remaining tides are substantially smaller, but nevertheless reach signal magnitudes that are considered relevant in view of the high sensitivity of the new Laser Ranging Interferometer (LRI) on GRACE-FO (Ghobadi-Far et al., 2022). Signals at all other possible frequencies including N_2 and L_2 are even well below the smallest constituent S_6 that is considered here, and we deem them as non-significant.

A similar analysis for tidal signals in ocean bottom pressure from MPIOM reveals the dominance of S_2 at all spatial scales, which is explained by the generally higher resonance of the geometry of major ocean basins at this period. When contrasted with the degree variance from atmospheric tide waves, the oceanic components
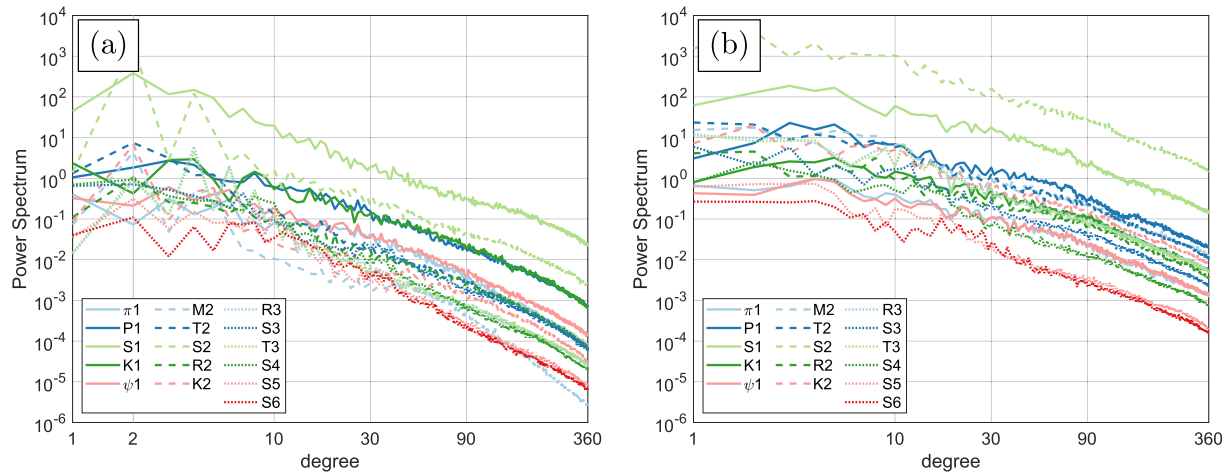
Figure 1. Degree variances of the amplitudes $\left(A_j = \left(C_j^2 + S_j^2\right)^{.5}\right)$ of 16 tidal waves in atmospheric surface pressure from ERA5 (a) and ocean bottom pressure from MPIOM (b) as listed in Table 1. Diurnal waves are shown in solid lines, semi-diurnal waves are shown in dashed lines, and waves at the ter-diurnal band or higher are shown in dotted lines.

feature comparatively large variances at the lowest spatial scales. Please, note that to avoid manifestations of the Gibbs phenomenon (e.g., artificial "ringing") on the degree variances and the potential corruption of the results, we have extrapolated the ocean fields inland prior to estimating the Stokes coefficients. From the numerous approaches that may be used to fill the points that lie in the transition zone (nodes with a land designation close to the coast) (e.g., see Albertella et al., 2008), we chose to solve this boundary value problem employing the parametric least squares collocation method (e.g., Kotsakis, 2007; Krarup, 1969) with Hirvonen's covariance functions controlling the signal decay with distance inland (see Equation S1 of Supporting Information S1 for further details). We observed that skipping this pre-processing step yields smaller energy decay rates per spherical degree, that is, $0.57\log_n\left(\sigma_n^2\right)$, on average over all waves discussed herein (see Figure 2), and slightly larger degree variance at wavelengths spanning between 100 and 300 km. We acknowledge that many waves are substantially smaller than S_2, but nevertheless recommend to consider them as well for satellite gravimetry in view of the systematic impact of unaccounted tidal variations on the final monthly mean gravity field in order to eventually reach the GRACE baseline accuracy.
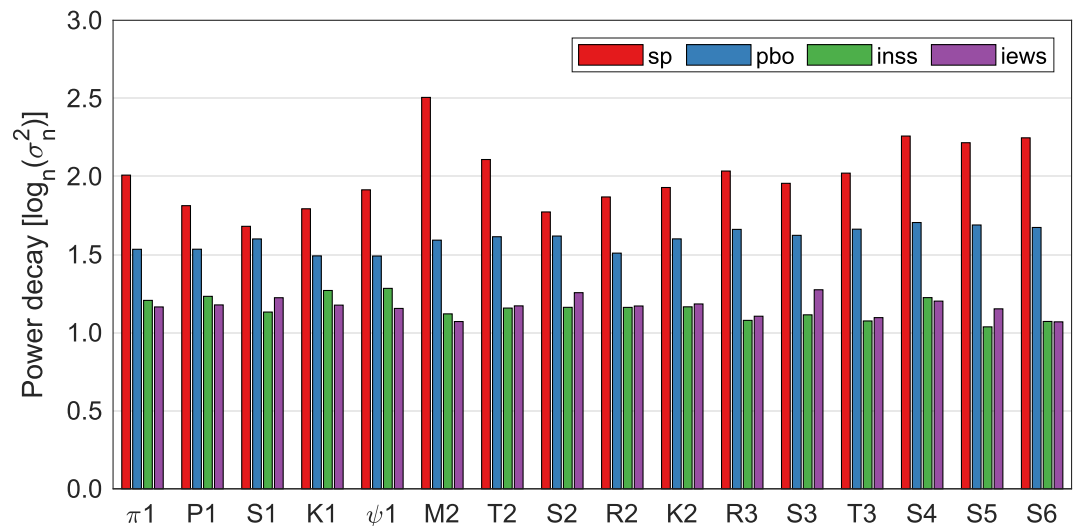

Figure 2. Wave-wise linear rate estimates for the decay of the harmonic amplitudes' energy per spherical harmonic degree, based on the associated degree variances (see Figure 1). The bars are grouped per wave and they refer to the atmospheric surface pressure (sp), the ocean bottom pressure (pbo), and the meridional (inss) and zonal surface wind stress (iews).
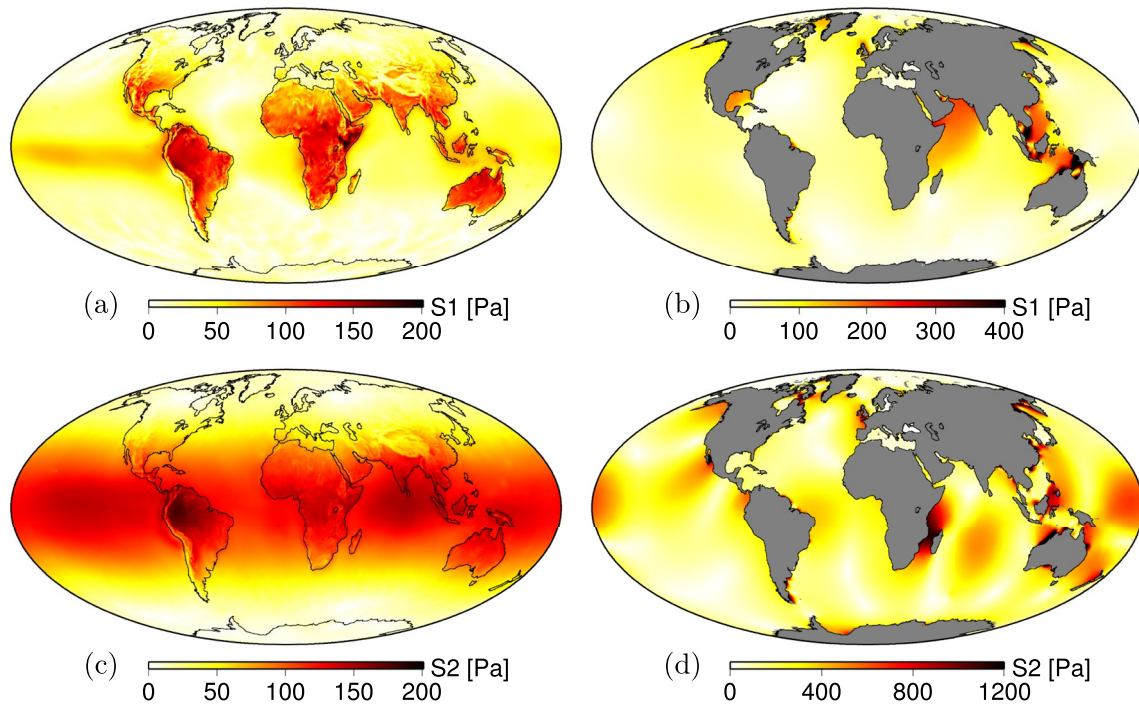
Figure 3. Harmonic amplitude for S_1 (top) and S_2 (bottom) in both atmospheric surface pressure from ERA5 (left) and ocean bottom pressure from MPIOM with ERA5 forcing (right) as obtained from a least squares estimation based on hourly data from 2007 to 2014.

To further characterize those degree variance spectra (σ_n^2, where n denotes spherical harmonic degree), we also estimate energy decay rates per spherical harmonic degree for the individual tidal waves (see Figure 2), which in essence is linearly approximating the wave-dependent degree variances illustrated in Figure 1. Highest rates of $2.5\log_n\left(\sigma_n^2\right)$ are found for atmospheric surface pressure at the M_2 frequency, which will be discussed in some more detail in the next Section. On the other hand, the decay rate is lowest for S_1, which can be related to the comparably high spatial variability for this tide in particular in the tropics. Energy decay rates are also calculated for ocean bottom pressure and surface wind stress in zonal and meridional direction (see Supporting Information S1), but do not show a prominent dependency on the wave's period.

For completeness, we note that a significant portion of periodic variations is also found at synoptic timescales that are much longer than the sub-daily periods considered in this paper. We thus find substantial spectral peaks at periods of the long-periodic tides (e.g., M_f, M_s, and S_{ta}). Those variations will not be considered further in this article, since (a) such signals are very well resolved from 3 hourly time-series of the non-tidal background model AOD1B, and (b) the oceanic response to such pressure fluctuations is almost perfectly compensated inverse-barometrically, so that those would not benefit from dedicated numerical modeling of ocean dynamics as attempted in this work.

4. Spatial Characteristics of Tides in ERA5 and MPIOM

Drawing from the methodology outlined above, we present the spatial distributions of the amplitudes for the major waves S_1 and S_2 in both atmosphere and ocean (Figure 3). The atmospheric tide S_1 as obtained from ERA5 is characterized by strong amplitudes over the continents that are particularly pronounced at low altitudes in the tropics. Mountain regions like the Tibetan Plateau or the Andes exhibit much lower amplitudes than regions at sea-level in similar latitudes. The atmospheric pressure signals over the ocean regions are much weaker. The picture is very different for S_2, which is dominated by a zonally symmetric westward-traveling wave centered at the equator (see Supporting Information S1 for a movie). Signals at polar latitudes, however, are almost non-existent for all waves considered.
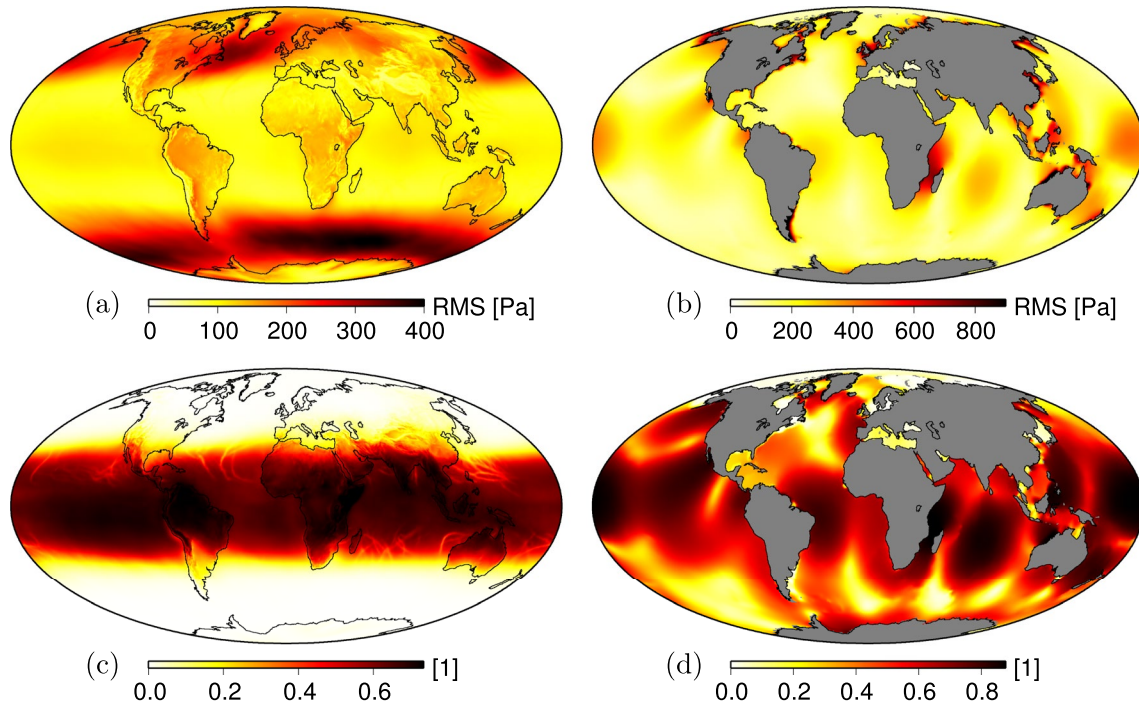
Figure 4. Scatter in the sub-daily frequency band (upper row) and the portion of these variations explained by the waves in Table 1 (lower row). Depicted are quantities for atmospheric pressure (left) and ocean bottom pressure (right). Note the different colorbars.

For the ocean response, we note the excitation of basin-wide oscillations for both S_1 and S_2 that lead to enhanced bottom pressure variations in coastal regions. Particularly the Indian Ocean has several areas that are very resonant for either S_1 and S_2, but also other regions exhibit bottom pressure changes that are much larger than the atmospheric forcing itself. It is also worth mentioning that the oceanic response to atmospheric tides is not confined to the tropics but emanates well into the polar seas.

We now focus on the amount of variability at sub-diurnal time-scales that can be explained by the 16 selected tidal waves. For this the pressure data over all 8 years is high-pass filtered using a sixth order Butterworth filter with a cutoff frequency of 24 hr. In Figure 4 we show the RMS of the sub-daily variability for both surface pressure and ocean bottom pressure together with the fraction of the signal explained by the sum of all 16 waves. Wind stress harmonics are illustrated in Figure S3 (meridional component) and Figure S4 (zonal component) of Supporting Information S1, and Figures S8 and S9 in Supporting Information S1 show the high-frequency variability explained by the 16 partial tides for the wind stress components.

For atmospheric surface pressure, sub-daily variability is most pronounced in the west wind regimes of the moderate latitudes in both hemispheres, where cyclonic systems are advected with the mean flow and thus cause rapidly changing surface pressure values in particular at times of the passage of an atmospheric front. These synoptic signals cannot be explained by the wave ensemble employed, whatsoever. On the other hand, sub-diurnal variability in the tropics is much weaker (just around 10 Pa), but can be very well explained by the sum of 16 tidal waves with up to 70% for $|\varphi| < 10°$. The variance portion may be approximated by a Gaussian function of $\cos(\varphi)$ with full width at half maximum of roughly 56° about the equator. Therein, evident are tropical cyclone tracks in the Tropics of Cancer and Capricorn.

We also assess the individual contribution of each wave in post-fit residual scatter reduction. For atmospheric pressure, S_1 dominates in the diurnal band $\left(\overline{\kappa}_{sp}^{S_1} = 4.2\%\right)$ and S_2 dominates in the semi-diurnal band $\left(\overline{\kappa}_{sp}^{S_2} = 22.7\%\right)$. While S_2 pressure oscillations have a larger amplitude over the ocean as well as for most area over land, there are clusters where S_1 amplitudes exceed 1.5 hPa (Ethiopian Highlands and Northern Andes). In the ter-diurnal band, the contributions of S_3 are exceeded by those of its side bands R_3 and T_3 by at least a factor of two individually $\left(\overline{\kappa}_{sp}^{R_3|T_3} = 0.2\%\right)$.

It is worth recalling that surface pressure in atmospheric reanalyzes is tightly constrained by pressure readings from in situ barometers that are attached to the crust or to buoys floating at the sea-surface. Such instruments are, however, subject to vertical displacements induced by crustal deformations arising from body tides of the solid Earth, or ocean tides in the case of floating instruments. Vertical motions of a barometer in an otherwise undisturbed atmosphere would induce changes in pressure readings in line with the hypsometric equation. We quantify those subtle harmonic oscillations that are not considered in the assimilation process, thus giving rise to spurious tidal harmonics and potential discrepancies while comparing model-derived tidal harmonics to products (e.g., from space geodesy) where astronomical forcing has been thoroughly considered.

Following the latest IERS Conventions (Petit & Luzum, 2010), employing the DE440 ephemerides (Park et al., 2021), and the fully fledged (linear, non-linear, and long-period components) sea surface height variations predicted from FES2014b (Lyard et al., 2021) we calculate crustal displacements and sea tide elevations induced by lunisolar gravitational attraction. We obtain the expected pressure variations from the hypsometric equation

$$p(\varphi, \lambda, dh) = p(\varphi, \lambda, s) \left(\frac{t(\varphi, \lambda, s) - \gamma(\varphi, \lambda) dh}{t(\varphi, \lambda, s)} \right)^{\frac{g(\varphi, s)}{R\gamma(\varphi, \lambda)}}, \tag{5}$$

where p denotes pressure, t denotes temperature, g is the gravitational acceleration, γ is the temperature lapse rate, dh is the height difference between the point of interest and the orography s, and R is the specific gas constant for dry air. Afterward, we perform a harmonic analysis on them following the strategy presented in Section 3 and adopting reference pressure and reference temperature from averaging the related monthly ERA5 surface fields. Over land, pressure harmonics do not differ more than 2 Pa with the anomalies ranging 0.9–6.8 Pa. The global wave-wise root-mean-square (RMS) is 0.6 Pa for M_2, 0.3 Pa for S_2, and 0.2 Pa for K_1, and the global RMS of the anomalies is 0.4 Pa. These pressure anomalies decrease with increasing distance from the equator and decrease with increasing altitude. However, the spurious pressure anomalies have a global average RMS of 1.8 Pa over the oceans. In particular, the waves for which these spurious variations have the largest amplitude are M2 (2.5 Pa), S_2 (1.0 Pa), and K1 (0.9 Pa). The spatial patterns for S_1 and S_2 (see Figure 5) are similar to those of K_1 and M_2, respectively, owing to the proximity in terms of frequency.

5. Ocean Tide Simulations With Atmospheric Forcing From TiME

For all 16 tidal waves identified above, we further employ the Tidal Model forced by Ephemerides (TiME) (Sulzbach et al., 2021; Weis et al., 2008), a barotropic ocean tide model, that benefits from a much higher spatial resolution and more elaborate tidal dissipation mechanisms when compared to MPIOM. The TiME model numerically integrates the shallow water equations (SWE) on a $\frac{1}{12}°$ meshgrid, describing the ocean state by its free surface elevation ζ and its depth averaged velocity $\mathbf{v} = \begin{bmatrix} ccu & v \end{bmatrix}^\top$. The atmospheric forcing is considered by modifying the momentum balance component of the shallow water equations (Gill, 1982), now reading

$$\partial_t \mathbf{v}^\omega = -\nabla \left(g\zeta^\omega - g\zeta_{SAL}^\omega (\zeta^\omega) - V_g^\omega + V_p^\omega - V_l^\omega - V_o^\omega \right) + \mathbf{W}^\omega + \hat{R}\mathbf{v}^\omega. \tag{6}$$

Here, $g = 9.80665$ m s^{-2} is the WMO-defined surface gravity acceleration, ∇ is the horizontal Nabla-operator, $g\zeta_{SAL}^\omega$ is the Self-Attraction and Loading (SAL) potential of the anomalous ocean mass distribution, V_g^ω is the gravitational tide-raising potential, that we evaluate as partial potential of a given frequency ω, with the decomposition of Hartmann and Wenzel (1995). This partial tide forcing induces a dynamic response that converges to a temporal harmonic behavior in ζ^ω and $\mathbf{v}^\omega$, where we neglect minor-amplitude higher harmonic contributions introduced by nonlinearity. Residual accelerations including dissipative effects, Coriolis and advective acceleration are comprised in the operator $\hat{R}$. In addition to these effects, atmospheric forces are considered.

The most significant atmospheric acceleration is exerted by direct pressure forcing $V_p^\omega = y^\omega \rho_{sw}^{-1}$, where y^ω is the planetary surface pressure variation by a single partial wave defined in Equation 2. Since a positive pressure variation represents a repulsive potential for the ocean, the sign of V_p^ω is inverted with respect to V_g^ω, that by definition exerts attractive forces. Furthermore, there are secondary effects induced by surface pressure variations that act upon the solid Earth, inducing a corresponding back-action on the ocean. This is true for dry land as well as the solid Earth below the oceans. Therefore, we introduce the potentials V_l^ω and V_o^ω, that represent the effects of
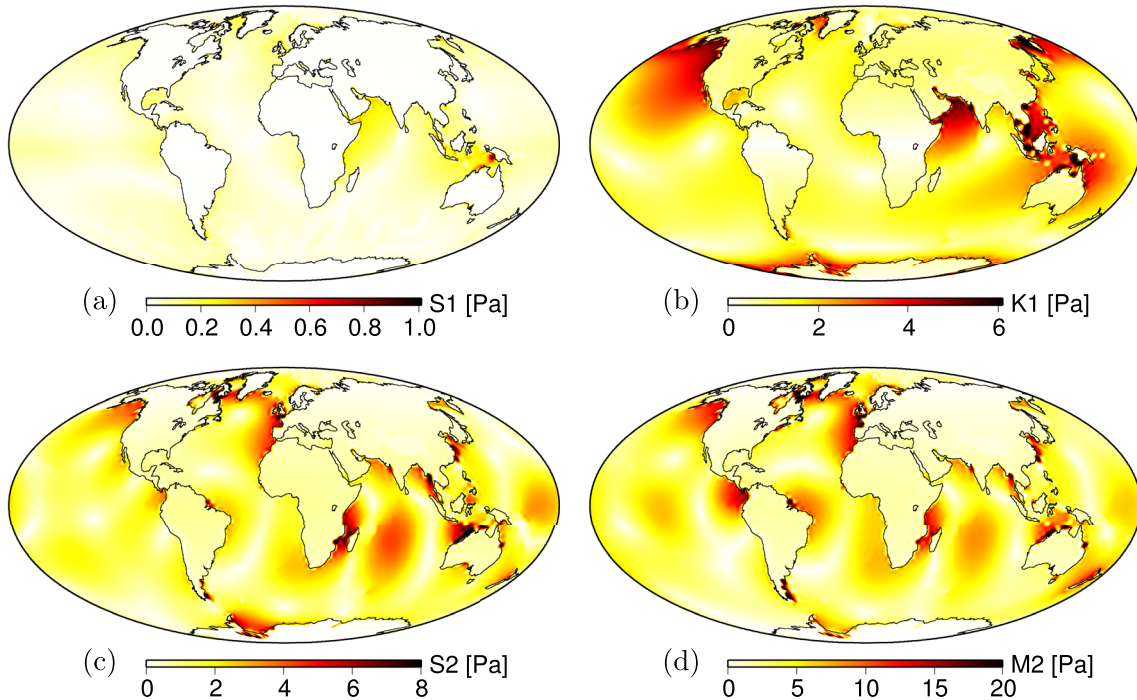
Figure 5. Harmonic pressure variations excited solely by vertical shifts of the lower boundary of the atmosphere at the Earth's crust induced by solid Earth tides, and at the sea surface induced by ocean tides.

Self-Attraction and Loading induced by V_p^ω over land and oceans, respectively. They are obtained by evaluating (e.g., Kuhlmann et al., 2011; Schindelegger et al., 2018)

$$V_{l/o}^\omega(\mathbf{x}) = \frac{3\rho_{sw}}{\rho_{se}} \sum_n \frac{\alpha_n}{2n+1} v_{l/o}^n(\mathbf{x}) \tag{7}$$

where $\rho_{sw} = 1{,}024$ kg m^{-3} is the mean density of sea water, $\rho_{se} = 5{,}510$ kg m^{-3} is the mean density of the solid Earth, $\alpha_n = 1 + k_n - h_n$ is combination of load Love numbers from PREM (Dziewonski & Anderson, 1981; Wang et al., 2012), and $\sum_n v_{l/o}^n(\mathbf{x})$ is the decomposition of $V_p^\omega \cdot M_{l/o}$ into a set of real-valued spherical harmonic functions Y_{nm}, degree-wise comprised to $v_{l/o}^l$, with $M_{l/o}$ being the mask comprising wet (o), or dry (l) grid cells. While the former contributions represent barotropic, curl-free gradient forces, the turbulent wind stress acceleration $\mathbf{W}^\omega = \mathbf{w}^\omega H^{-1} \rho_{sw}^{-1}$ includes a rotational and a gradient component, that can be distinguished by conducting a Helmholtz decomposition. Here $\mathbf{w}^\omega$ is the turbulent surface wind-stress and H is the bathymetric depth. For the following simulations, TiME was employed in partial tide forcing mode, with a timestep of 180 s and an initialization time of 30 days, before harmonic constituents $\zeta^\omega = \zeta_{\cos}^\omega \cos(\omega t) + \zeta_{\sin}^\omega \sin(\omega t)$ were extracted. By comparing $\zeta_{\cos/\sin}^\omega$ to the respective constituents derived from tide gauge data sets or satellite data-constrained tidal atlases in terms of an RMS metric, the model performance can be quantified with respect to the tidal mean signal that we define as the mean quadratic amplitude measured at the tide gauge stations.

5.1. Excitation Mechanisms of the S_1-Tide

To distinguish the influence of the individual tide-raising forces described in Equation 6 we perform a number of simulations for the solar S_1-tide that is dominated by atmospheric excitation but also exhibits a minor gravitationally excited component. Oceanic responses induced by direct atmospheric pressure forcing (PRDIR), the secondary effects of SAL over continents (SALL) and oceans (SALO), as well as the excitation by wind stress (WIND) and gravitational excitation (GRAV) are displayed in Figure 6 alongside with the respective barotropic potentials induced by atmospheric pressure. We note that GRAV is corrected for the recent phase of the solar perigee (cycle of 20,942 years) as in Ray and Egbert (2004). The ocean response is dominated by the direct pressure forcing, with small deviations originating from secondary effects that are smaller by a factor of 5–10, which is in
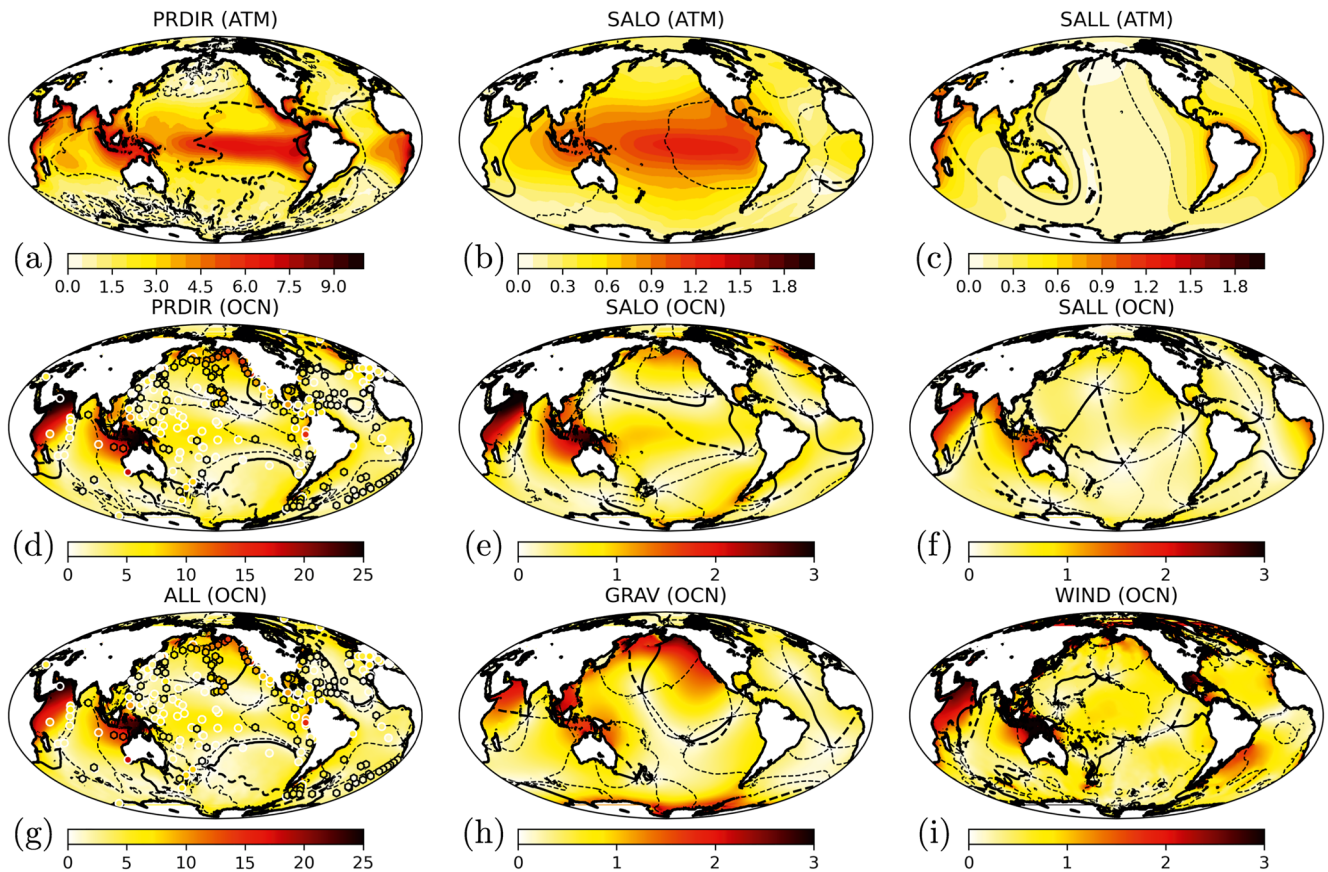
Figure 6. Top row: Atmospheric S_1-forcing potential expressed as equivalent sea water height (mm) for (a) direct pressure forcing (PRDIR), (b) SAL-potential over the ocean (SALO), and (c) SAL-potential over the continents (SALL). Even though the three fields are defined on a global domain, they are whited out over the continents, since only barotropic forces in the ocean impact the ocean tides. Middle row: Respective barotropic ocean response amplitude to pressure forcing (d), SAL over the oceans (e), and SAL over the continents (f). Bottom row: Ocean response amplitude to gravitational forcing (h), wind stress forcing (i), and all effects combined (g). Tidal phases are displayed as contours in increments of 60° (0°: bold, 60°: bold, dashed), in the phase convention of Doodson and Schureman as outlined in Appendix A of Ray and Egbert (2004). Ocean bottom pressure stations (black hexagons) and tide gauge stations (white circles) that were used for model validation (see Table 2) are presented for PRDIR and ALL.

line with the findings of Schindelegger et al. (2016) and Ray and Egbert (2004) who concluded that secondary effects will be of minor impact. Comparing the amplitude and phase-pattern of the individual effects we find that the SALO and PRDIR responses are similar, but with a phase shift of approximately 180°, which was to be expected from the respective forcing patterns and the definition of the SALO-potential. On the other hand, the continental SAL-response, SALL, shows an altered ocean response with amplitude patterns that are related to the exciting forces concentrated at the equatorial coasts. The same is true for the GRAV-response that exhibits the typical admittance pattern of a diurnal degree-2 tide, as well as for the wind-stress-induced tide, WIND, where ocean responses are strongest in near-coastal, shallow-water regions. Nonetheless, we want to emphasize that all discussed individual effects show long-wavelength dominated patterns that are typical for ocean dynamics mediated by near-diurnal oceanic normal modes (Müller, 2007).

While numerical modeling experiments allow the separate assessment of single effects, real observations (e.g., tide gauge and satellite altimetry data) cannot distinguish between individual excitation mechanisms as they oscillate at the same frequency. Therefore, it is a reassuring result for the presented modeling considerations that comparison with tide gauge data shows the best agreement as measured by RMS-metrics when including all discussed effects (see Table 2). While the results for intercomparison with the satellite data-constrained FES14-atlas are similar, the best agreement is achieved when excluding the secondary effects, thereby hinting toward to the omission of those processes in the FES14 model simulations.

Table 2

Root Mean Square Deviation in cm for Selected TiME and FES14 Solutions With Respect to Independent Data Sets Comprising Tides S_1 to S_4 With Different Combination of the Discussed Effects

Tide	TICON	Ray (2013)	FES14
S_1 (Signal)	0.47	0.41	
S_1 (ALL)	**0.28**	**0.29**	0.13
S_1 (noGRAV)	**0.28**	0.31	0.14
S_1 (noSAL)	0.40	0.30	**0.11**
S_1 (noWIND)	0.30	**0.29**	0.12
S_1 (FES14)	0.33	0.30	
S_2 (Signal)	12.24	10.95	
S_2 (ALL)	**6.26**	**1.62**	**1.62**
S_2 (noATM)	6.32	1.80	**1.62**
S_3 (Signal)	0.11		
S_3 (ATM)	0.09		
S_4 (Signal)	0.07		
S_4 (ATM)	0.11		

Note. ATM comprises all atmospheric effects. The employed data sets stem from ocean bottom pressure stations complied by Ray (2013), and the tide gauge data set TICON (Piccioni et al., 2019), where only stations of the subset TICON-td were considered (Hart-Davis et al., 2022). Further, the deviation between TiME and FES14 (Lyard et al., 2021) in non-Polar (|latitude| < 66°), open ocean (depth >1,000 m) areas is listed in the third column. This value signifies the deviation between FES14 and the respective TiME-experiment and is thus not a direct indication of the accuracy of both models with respect to an external data set. The smallest value per column for S_1 and S_2 is presented in bold font.

5.2. Oceanic Response at Higher Frequencies

We also discuss the results for a number of partial tides with semidiurnal and higher frequencies referring to Table 2 and Figure 7 for the discussion.

While the semidiurnal S_2 tide is dominated by the gravitational forcing, it comprises a significant contribution excited by atmospheric effects, that is, the atmospheric forcing is known to possess approximately 15% of the gravity forcing amplitude (Arbic, 2005). In contrast to the S_1 ocean tide, where the individual contributions by atmospheric and gravity forcing exhibit characteristic response patterns (compare Figures 6d–6i and Ray and Egbert [2004]), both S_2-effects excite nearly identical ensembles of ocean normal modes (e.g., Müller, 2007) with a phase shift of approximately 110° (Arbic, 2005). This causes an apparent amplitude-decrease, and phase shift of the S_2-tide with respect to ignoring the atmospheric forcing as already reported by Cartwright and Ray (1994). These results are reproduced by the presented simulations. Further, we find that the RMS with respect to the employed tide-gauge ensembles is smaller when including atmospheric effects. This indicates the correct depiction of atmospherically induced dynamics for the S_2-tide.

Gravitational excitation of the terdiurnal S_3-tide is negligible. On the other hand that the annual satellites of S_3, that is R_3 and T_3, induce a prominent annual modulation of this terdiurnal triplet (Ray & Poulose, 2005). Our simulations reproduce these results, showing an increased amplitude for T_3 and R_3 up to 4 mm, with similar ocean response patterns, but shifted by 180°. While the RMS-values are larger with respect to the tidal signal than they were for S_1 and S_2, one still finds RMS < signal, indicating the correct prediction of a certain fraction of the tidal dynamics.

This changes for the S_4-tide, where the RMS is larger than the mean signal. Reasons for the increase of the RMS to signal fraction could be the generally smaller signal of the considered ocean response, that makes it harder to determine both the forcing fields and the tide gauge constituents. The high
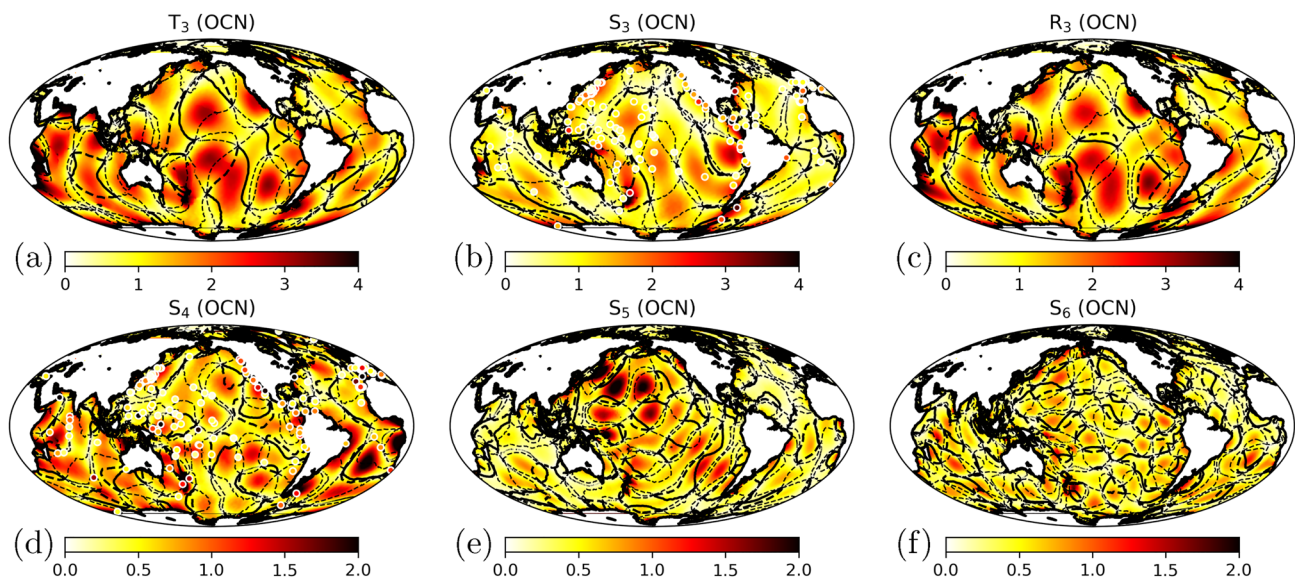

Figure 7. Ocean response in sea surface height (mm) to atmospheric forcing for partial tides listed in Table 1 with terdiurnal and higher frequencies. Top row: The terdiurnal S_3-triplet (T_3, S_3, R_3) is dominated by its annual satellites. Bottom row: Higher frequency tides (S_4, S_5, S_6) are increasingly less resonant with smaller amplitudes. The inserted points represent tide gauge amplitudes of TICON.

frequency tides might also be prone to a stronger variability of the atmospheric forcing. Another reason for worse agreement at S_4 frequency is the neglection of the non-linear, shallow-water interaction of S_2 with itself in our experiment, that induces S_4 oscillations, that is, $S_2 + S_2 \rightarrow S_4$. While this contribution is expected to be of similar magnitude as the atmospheric S_4-component (approximately $\frac{1}{4}$ of M_4, the most-prominent shallow-water tide), shallow-water tides are currently not sufficiently accurately predicted with TiME. Therefore the component was ignored after initial tests. We conclude the discussion of the S_4-results by remarking that the poorer performance for very high frequency tides, could also partially originate from the optimization of TiME for semidiurnal and diurnal tides.

The additionally displayed results for S_5 and S_6 confirm the tendency of a further decreasing ocean tide amplitude as well as more finely structured amphidromic systems due to the higher oscillation frequencies. As the spatial excitation pattern of the pressure forcing is also fine structured, the oceanic response is not as close to resonance as one finds for diurnal and semidiurnal tides that are known to resonantly excite oceanic normal modes.

5.3. Comparison of TiME and MPIOM Solutions

As discussed in the previous subsections, the successful implementation of the proposed atmospheric excitation mechanisms into TiME lead to a reduction of the introduced RMS-metrics with respect to tide gauge data sets (compare Table 2).

On the other hand, atmospherically induced oceanic tides are also excited indirectly in the MPIOM-runs if not priorly excluded from forcing fields and can be extracted by means of a harmonic analysis (see Section 3). As MPIOM is a baroclinic ocean model that is not optimized for the simulation of barotropic oceanic tides and features a much lower resolution, we expect the excited ocean tidal dynamics to agree less accurately with real data, for example, to exhibit a larger RMS-deviation. As MPIOM provides ocean bottom pressure variations δp only, while the employed tidal models TiME, FES and the TG-constituents are given in Sea surface height variations $\delta\zeta$, we convert between these quantities by evaluating

$$\delta p = \delta\zeta g \rho_{sw}. \tag{8}$$

We consider the MPIOM-solutions for S_1 and S_2 as they have the largest mean signal of the considered ensemble of tides. We further note that these simulations do not include the gravity excited contribution as outlined in Section 5.1 (MPIOM was not forced with the lunisolar gravity potential). We calculate the RMS for these solutions with respect to the open ocean TG-ensemble of Ray (2013) where we employ the pure MPIOM-solution (no gravity forcing) for S_1 and add the gravity excited contribution obtained from TiME to the MPIOM-solution for S_2. This results in an RMS of 1.73 cm for S_2 and 0.42 cm for S_1, which implies an RMS-increase of +0.11 cm compared to the corresponding TiME-solutions (RMS = 1.62 and 0.31 cm, respectively). This comparison suggests that the simulation of atmospherically excited tidal dynamics is considerably more accurate with a dedicated barotropic ocean tide model as TiME. We thus convert results from TiME for all 16 partial tides listed in Table 1 into Stokes coefficients for the direct application of this data as a new tidal background model in GRACE-FO data analysis.

6. Application in GRACE-FO Gravity Field Processing

In-phase and quadrature components for 16 waves in the atmosphere from ERA5 (see Table 1) and a subset thereof consisting of 10 waves in the oceans from TiME, namely, π_1, S_1, ψ_1, T_2, R_2, T_3, S_3, R_3, S_5, and S_6, as given in Stokes coefficients expanded to degree and order 100 are now being tested in GRACE-FO global gravity field estimation. Our analysis is based on pre-fit residuals of LRI range-accelerations obtained after precise orbit determination of the data screening step as performed during the GFZ RL06 processing (Dahle et al., 2019). Since the primary observation type is range-rate, range-acceleration residuals are computed by differentiating range-rate residuals applying a fifth order Butterworth low-pass filter with a cut-off frequency of 1/60 Hz. Subsequently, the residuals are binned into equiangular 3° cells and the standard deviation for each cell is computed (see Figure 8). As improvements in the background modeling will lead to a better fit with the measured observations in orbit and gravity field adjustment, that is, smaller values in the reduced observations vector, the size of variability in observation residuals indicates whether a certain set of background models represents high-frequency variations better compared to another model ensemble.
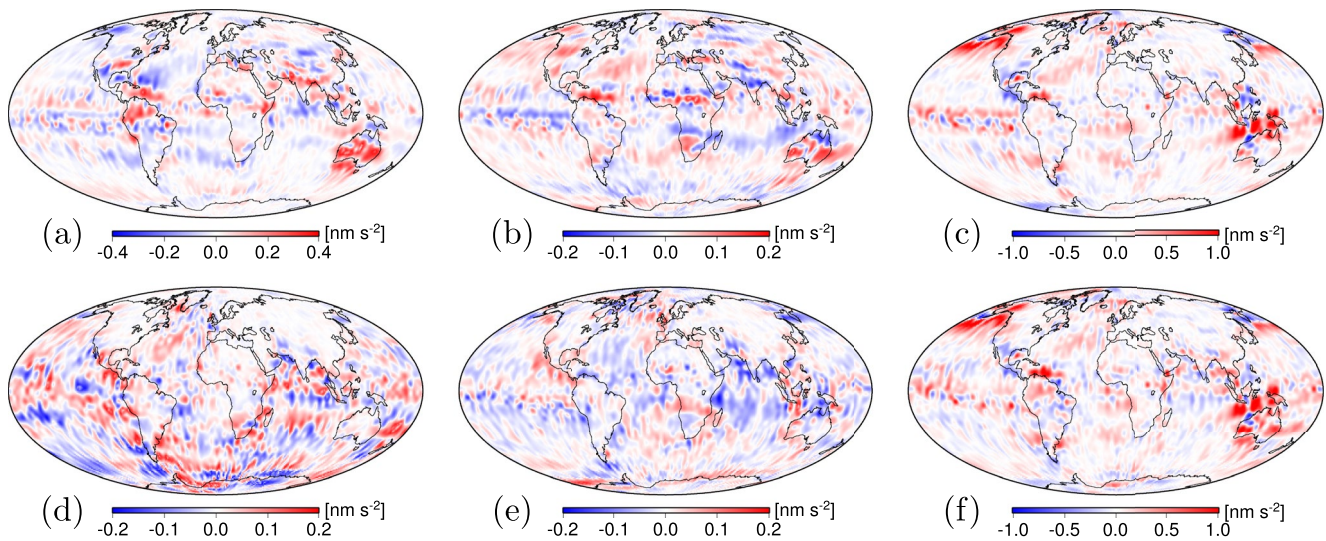
Figure 8. Scatter difference between LRI range-acceleration pre-fit residuals, binned in equiangular 3° cells. Shown are the differences (a) C0 - C1, (b) C1–C2, (c) C2–C3, (d) C3–C4, (e) C4–C5, and (f) C0–C5. Red indicates improvements in the solution with the highest index. Blue indicates deterioration. Note the different colorbar ranges across the panels.

As a reference case (C0), we use the GFZ RL06 background models, that is, the FES2014 ocean tide model (Lyard et al., 2021) and the model of Biancale and Bode (2006) for atmospheric tides. Note that the latter Biancale and Bode (2006) contains only the two main tidal constituents S_1 and S_2 up to degree 8 and order 5. To individually assess the impact of the different tides derived in this study, the following cascade of experiments has been conducted employing all GRACE-FO LRI observations collected during January 2019:

C0: high-frequency tidal variability as in GFZ RL06 (Dahle et al., 2019);

C1: high-frequency tidal variability as in C0, but with atmospheric tides S_1 and S_2 from this study instead of Biancale and Bode (2006);

C2: high-frequency tidal variability as in C1, but with the 14 additional atmospheric tides from this study;

C3: high-frequency tidal variability as in C2, but ocean tide S_1 from FES2014b replaced by S_1 from this study (TiME);

C4: high-frequency tidal variability as in C3, but additionally with ocean tides T_3, S_3, R_3, S_5, and S_6 from this study; note that these five waves are neither contained in FES2014b nor interpolated by admittance in our software EPOS-OC; and

C5: high-frequency tidal variability as in C4, but ocean tide waves T_2 and R_2 from FES2014b replaced by T_2 and R_2 from this study and additionally with ocean tides π_1 and ψ_1; note that the latter two tides are not contained in FES2014b, but interpolated by admittance in our software.

We note that the improvement (red in Figure 8) or deterioration (blue in Figure 8) in terms of pre-fit residuals shows very small correlation with the magnitude of the residuals (less than 0.08 in all experiments carried out herein), which suggests that the scatter of the pre-fit residuals may be associated with the local performance of the models. Pre-fit residuals over land are most probably associated with hydrological mass anomalies, however, since we study the differences between the different scenarios (C0–C5) we expect the influence of hydrological signals to cancel out. Applying the atmospheric tide amplitudes for S_1 and S_2 estimated from ERA5 in lieu of those provided by Biancale and Bode (2006) yield an average improvement of 0.004 nm s^{-2} (0.1%) in the binned LRI residuals. Locally, changes can reach up to 0.5 nm s^{-2}, which corresponds to an improvement of 31% in the area around Australia. The improvement over land is much larger compared to the ocean (0.6%), what we attribute to the orographic features in S_1 and their appropriate representation by the higher spherical harmonic expansion employed in this work. The improvement stemming from employing all 16 waves tabulated in Table 1 is on average 0.003 nm s^{-2} (0.2%) which demonstrates that considering an atmospheric tide model featuring more waves many of which at higher frequencies, in addition to the S_1 and S_2, is justified. We find the largest improvements (up to 12%) in western Australia, the Caribbean Sea, as well as the continental western North America. Utilizing the S_1 ocean results from TiME (Sulzbach et al., 2021) in lieu of FES2014b yields a global average improvement

of 1.7% (0.041 nm s^{-2}). The residual scatter reduces down to more than 50% in the Banda and Arafura Seas north of Australia, as well as in the Caribbean Sea and the Gulf of Alaska. The largest contribution to this improvement stems from ocean cells where the scatter reduction is larger by 2.3%. While we note a deterioration along the Central American trench, we cannot attribute it to the spatial representativeness due to the high-resolution grid employed in the TiME simulations. In scenario C4 where we model variability at five sub-diurnal frequencies neither included in FES2014b nor interpolated by admittance during the reduction of GRACE-FO observations, we find an average improvement of 0.1% (0.004 nm s^{-2}), which suggests that the effect of the ocean mass redistribution of these ocean tidal waves to the GRACE-FO observations is very small. Even though it appears theoretically advantageous to include those minor tides explicitly as background models into the GRACE-FO gravity field inversion process, our current results do not allow for a clear recommendation. Further study is thus needed to carefully assess the potential benefit of those smaller ocean tides as modeled by TiME. Adopting the semi-diurnal waves T_2 and R_2 from TiME instead of FES2014b and including ψ_1 and π_1 from TiME (C5) yields a slight deterioration, on average (0.2% - 0.003 nm s^{-2}). The fact that this occurs predominantly over the open ocean suggests that the assimilation of actual altimetric observations (FES2014b) cannot be substituted only by astronomical and weather forcing (TiME) for those tides. Especially ψ_1 is known to be especially difficult to model and estimate due to a multitude of effects (gravitational and radiational components, coincidence with a compound tide, and manifestation of seasonal modulation in K_1) influencing the ocean response (e.g., Ray et al., 2021).

7. Summary and Conclusions

GRACE and GRACE-FO observations provide unique estimates of mass transport within Earth's fluid envelope that are of particular importance for the precise monitoring of changes in continental ice masses and groundwater resources. The specific processing approach of satellite gravimetry which accumulates sensor data over 30 days to solve for a single monthly mean gravity field requires the careful modeling of high-frequency mass variability in order to avoid the introduction of temporal aliasing artifacts. This also includes atmospheric tides and their oceanic response, which have been reassessed in this paper from ERA5, the latest global reanalysis of ECMWF.

In contrast to previous work by Dobslaw et al. (2017), we find 16 waves as relevant in the context of satellite gravimetry. The selection even includes variations at the S_6 period, which have not been accessible from previous atmospheric data sets sampled at 3-hourly intervals only. We also recommend that N_2 and L_2 not be further considered in the atmospheric tide ensemble, since we found those signals to be negligibly small when compared to other waves.

For all 16 selected partial tides, dedicated simulations with the high-resolution shallow-water code TiME have been performed. Sensitivity experiments underline the relative importance of various interfering forcing agents in particular for the S_1 ocean tide. Minimal errors with respect to in situ tide gauge data are obtained when all different effects from surface pressure, wind stress as well as self-attraction and loading are taken into account. In addition, we find that the accuracy of the TiME experiments is generally higher than corresponding tidal estimates obtained from a recent MPIOM experiment. This is plausible in view of the higher resolution and the more elaborate dissipation mechanisms employed in TiME.

The new models for atmospheric (from ERA5) and ocean tides (from TiME) have been also applied as background models in data analysis experiments with real GRACE-FO sensor data for an individual month of the year 2019. The evaluation of pre-fit residuals reveal that implementing the new models for S_1 has a positive impact with respect to the background models previously applied in latest available release 06 of the GRACE and GRACE-FO gravity fields published by GFZ. Results for the smaller tides are less conclusive, but further progress is expected as soon as the benefits of the new LRI instrument operated on GRACE-FO as a technology demonstrator (Ghobadi-Far et al., 2022) are fully utilized also in the gravity field estimation. It is further planned to remove signals from all 16 waves discussed in this paper from the next release (RL07) of Atmosphere and Ocean De-Aliasing Level-1B product (Shihora et al., 2022), so that those coefficients only represent non-tidal variability and can be used in combination with the tidal models presented here.

Data Availability Statement

ECMWF's ERA5 surface and model level data are publicly available, and may be retrieved employing the cdsapi (https://pypi.org/project/cdsapi/). The ocean-sea ice component of the MPI-ESM, MPIOM, is publicly available (https://mpimet.mpg.de/en/science/models/mpi-esm/mpiom). Tide gauge data employed herein are publicly available from (Piccioni et al., 2019). GRACE-FO observations are available under (https://doi.org/10.5067/graod-1bg06). Calculations carried out herein were facilitated by employing the Climate Data Operators software suite (schulzweida, 2022). All maps in the manuscript have been created employing the Generic Mapping Tools (Wessel, 2019). Stokes coefficients for all 16 selected waves in the atmosphere (from ERA5) as well the corresponding ocean tides (from TiME, forced in part by ERA5) are publicly available under (Sulzbach et al., 2022).

References

Albertella, A., Savcenko, R., Bosch, W., & Rummel, R. (2008). *Dynamic ocean topography—The geodetic approach* (1st ed.). Technische Universität München Ingenieurinstitut für Astronomische und Physikalische Geodäsie.

Arbic, B. K. (2005). Atmospheric forcing of the oceanic semidiurnal tide. *Geophysical Research Letters*, *32*(2), L02610. https://doi.org/10.1029/2004GL021668

Biancale, R., & Bode, A. (2006). *Mean annual and seasonal atmospheric tide models based on 3-hourly and 6-hourly ECMWF surface pressure data*. Deutsches GeoForschungsZentrum GFZ. https://doi.org/10.2312/GFZ.B103-06011

Cartwright, D. E., & Ray, R. D. (1994). On the radiational anomaly in the global ocean tide with reference to satellite altimetry. *Oceanologica Acta*, *17*(5), 453–459.

Chapman, S., & Lindzen, R. S. (1970). *Atmospheric tides*. Springer Netherlands. https://doi.org/10.1007/978-94-010-3399-2

Dahle, C., Murböck, M., Flechtner, F., Dobslaw, H., Michalak, G., Neumayer, K., et al. (2019). The GFZ GRACE RL06 monthly gravity field time series: Processing details and quality assessment. *Remote Sensing*, *11*(18), 2116. https://doi.org/10.3390/rs11182116

Dee, D. P., Uppala, S. M., Simmons, A. J., Berrisford, P., Poli, P., Kobayashi, S., et al. (2011). The ERA-Interim reanalysis: Configuration and performance of the data assimilation system. *Quarterly Journal of the Royal Meteorological Society*, *137*(656), 553–597. https://doi.org/10.1002/qj.828

Dieminger, W., Hartmann, G. K., & Leitinger, R. (1996). Atmospheric tides. In *The upper atmosphere* (pp. 97–109). Springer Berlin Heidelberg. https://doi.org/10.1007/978-3-642-78717-1_3

Dobslaw, H. (2016). Homogenizing surface pressure time-series from operational numerical weather prediction models for geodetic applications. *Journal of Geodetic Science*, *6*(1). https://doi.org/10.1515/jogs-2016-0004

Dobslaw, H., Bergmann-Wolf, I., Dill, R., Poropat, L., & Flechtner, F. (2016). *Product description document for AOD1B release 06, rev. 6.0*. GFZ Potsdam. Retrieved from ftp://isdcftp.gfz-potsdam.de/grace/DOCUMENTS/Level-1/GRACE_AOD1B_Product_Description_Document_for_RL06.pdf

Dobslaw, H., Bergmann-Wolf, I., Dill, R., Poropat, L., Thomas, M., Dahle, C., et al. (2017). A new high-resolution model of non-tidal atmosphere and ocean mass variability for de-aliasing of satellite gravity observations: AOD1B RL06. *Geophysical Journal International*, *211*(1), 263–269. https://doi.org/10.1093/gji/ggx302

Doodson, A. T. (1921). The harmonic development of the tide-generating potential. *Proceedings of the Royal Society of London. Series A, Containing Papers of a Mathematical and Physical Character*, *100*(704), 305–329. https://doi.org/10.1098/rspa.1921.0088

Drijfhout, S., Heinze, C., Latif, M., & Maier-Reimer, E. (1996). Mean circulation and internal variability in an ocean primitive equation model. *Journal of Physical Oceanography*, *26*(4), 559–580. https://doi.org/10.1175/1520-0485(1996)026<0559:mcaivi>2.0.co;2

Dziewonski, A. M., & Anderson, D. L. (1981). Preliminary reference Earth model. *Physics of the Earth and Planetary Interiors*, *25*(4), 297–356. https://doi.org/10.1016/0031-9201(81)90046-7

Farrell, W. E. (1972). Deformation of the Earth by surface loads. *Reviews of Geophysics*, *10*(3), 761–797. https://doi.org/10.1029/RG010i003p00761

Flechtner, F., Neumayer, K.-H., Dahle, C., Dobslaw, H., Fagiolini, E., Raimondo, J.-C., & Güntner, A. (2015). What can be expected from the GRACE-FO laser ranging interferometer for Earth science applications? *Surveys in Geophysics*, *37*(2), 453–470. https://doi.org/10.1007/s10712-015-9338-y

Gelaro, R., McCarty, W., Suárez, M. J., Todling, R., Molod, A., Takacs, L., et al. (2017). The modern-era retrospective analysis for research and applications, version 2 (MERRA-2). *Journal of Climate*, *30*(14), 5419–5454. https://doi.org/10.1175/jcli-d-16-0758.1

Ghobadi-Far, K., Han, S.-C., McCullough, C. M., Wiese, D. N., Ray, R. D., Sauber, J., et al. (2022). Along-orbit analysis of GRACE follow-on inter-satellite laser ranging measurements for sub-monthly surface mass variations. *Journal of Geophysical Research: Solid Earth*, *127*(2), e2021JB022983. https://doi.org/10.1029/2021jb022983

Gill, A. E. (1982). Forced motion. In A. E. Gill (Ed.), *Atmosphere-ocean dynamics*, *International geophysics series* (Vol. 30). Academic Press. https://doi.org/10.1016/S0074-6142(08)60034-0

Godin, G. (1972). *The analysis of tides*. University of Toronto Press.

Gordeev, R. G., Kagan, B. A., & Polyakov, E. V. (1977). The effects of loading and self-attraction on global ocean tides: The model and the results of a numerical experiment. *Journal of Physical Oceanography*, *7*(2), 161–170. https://doi.org/10.1175/1520-0485(1977)007<0161:teolas>2.0.co;2

Hartmann, T., & Wenzel, H.-G. (1995). The HW95 tidal potential catalogue. *Geophysical Research Letters*, *22*(24), 3553–3556. https://doi.org/10.1029/95GL03324

Hart-Davis, M. G., Sulzbach, R., Dettmering, D., Thomas, M., & Seitz, F. (2022). TICON-td: Third-degree tidal constants based on gesla sea-level records from globally distributed tide gauges [Dataset]. Pangaea. https://doi.org/10.1594/PANGAEA.943444

Hassler, B., & Lauer, A. (2021). Comparison of reanalysis and observational precipitation datasets including ERA5 and WFDE5. *Atmosphere*, *12*(11), 1462. https://doi.org/10.3390/atmos12111462

Hendershott, M. C. (1972). The effects of solid Earth deformation on global ocean tides. *Geophysical Journal of the Royal Astronomical Society*, *29*(4), 389–402. https://doi.org/10.1111/j.1365-246X.1972.tb06167.x

Hersbach, H., Bell, B., Berrisford, P., Hirahara, S., Horányi, A., Muñoz-Sabater, J., et al. (2020). The ERA5 global reanalysis. *Quarterly Journal of the Royal Meteorological Society*, *146*(730), 1999–2049. https://doi.org/10.1002/qj.3803

Huang, L., Mo, Z., Liu, L., Zeng, Z., Chen, J., Xiong, S., & He, H. (2021). Evaluation of hourly PWV products derived from ERA5 and MERRA-2 over the Tibetan Plateau using ground-based GNSS observations by two enhanced models. *Earth and Space Science*, *8*(5), e2020EA001516. https://doi.org/10.1029/2020EA001516

Jungclaus, J. H., Fischer, N., Haak, H., Lohmann, K., Marotzke, J., Matei, D., et al. (2013). Characteristics of the ocean simulations in the Max Planck Institute Ocean Model (MPIOM) the ocean component of the MPI-Earth system model. *Journal of Advances in Modeling Earth Systems*, *5*(2), 422–446. https://doi.org/10.1002/jame.20023

Kaula, W. M. (1959). Statistical and harmonic analysis of gravity. *Journal of Geophysical Research (1896-1977)*, *64*(12), 2401–2421. https://doi.org/10.1029/JZ064i012p02401

Kim, J. R., Roesset, P. J., Bettadpur, S. V., Tapley, B. D., & Watkins, M. M. (2001). Error analysis of the gravity recovery and climate experiment (GRACE) mission. In *Gravity, geoid and geodynamics 2000* (pp. 103–108). Springer Berlin Heidelberg. https://doi.org/10.1007/978-3-662-04827-6_17

Kobayashi, S., Ota, Y., Harada, Y., Ebita, A., Moriya, M., Onoda, H., et al. (2015). The JRA-55 reanalysis: General specifications and basic characteristics. *Journal of the Meteorological Society of Japan. Ser. II*, *93*(1), 5–48. https://doi.org/10.2151/jmsj.2015-001

Kotsakis, C. (2007). Least-squares collocation with covariance-matching constraints. *Journal of Geodesy*, *81*(10), 661–677. https://doi.org/10.1007/s00190-007-0133-5

Krarup, T. (1969). *A contribution to the mathematical foundation of physical geodesy*. Geodætisk Institut. Retrieved from https://books.google.de/books?id=mP3cGAAACAAJ

Kuhlmann, J., Dobslaw, H., & Thomas, M. (2011). Improved modeling of sea level patterns by incorporating self-attraction and loading. *Journal of Geophysical Research*, *116*(C11), C11036. https://doi.org/10.1029/2011jc007399

Landerer, F. W., Flechtner, F. M., Save, H., Webb, F. H., Bandikova, T., Bertiger, W. I., et al. (2020). Extending the global mass change data record: GRACE Follow-On instrument and science data performance. *Geophysical Research Letters*, *47*(12), e2020GL088306. https://doi.org/10.1029/2020GL088306

Levitus, S., Antonov, J., & Boyer, T. (2005). Warming of the world ocean, 1955–2003. *Geophysical Research Letters*, *32*(2), L02604. https://doi.org/10.1029/2004GL021592

Lindzen, R., & Chapman, S. (1969). Atmospheric tides. *Space Science Reviews*, *10*(1), 3–188. https://doi.org/10.1007/bf00171584

Lyard, F. H., Allain, D. J., Cancet, M., Carrère, L., & Picot, N. (2021). FES2014 global ocean tide atlas: Design and performance. *Ocean Science*, *17*(3), 615–649. https://doi.org/10.5194/os-17-615-2021

Malakar, P., Kesarkar, A., Bhate, J., Singh, V., & Deshamukhya, A. (2020). Comparison of reanalysis data sets to comprehend the evolution of tropical cyclones over North Indian Ocean. *Earth and Space Science*, *7*(2), e2019EA000978. https://doi.org/10.1029/2019ea000978

Marsland, S., Haak, H., Jungclaus, J., Latif, M., & Röske, F. (2003). The Max-Planck-Institute global ocean/sea ice model with orthogonal curvilinear coordinates. *Ocean Modelling*, *5*(2), 91–127. https://doi.org/10.1016/S1463-5003(02)00015-X

Müller, M. (2007). The free oscillations of the world ocean in the period range 8 to 165 hours including the full loading effect. *Geophysical Research Letters*, *34*(5), L05606. https://doi.org/10.1029/2006GL028870

Park, R. S., Folkner, W. M., Williams, J. G., & Boggs, D. H. (2021). The JPL planetary and lunar ephemerides DE440 and DE441. *The Astronomical Journal*, *161*(3), 105. https://doi.org/10.3847/1538-3881/abd414

Petit, G., & Luzum, B. (2010). In *IERS conventions (2010)* (Vol. 36). Verlag des BKG.

Piccioni, G., Dettmering, D., Bosch, W., & Seitz, F. (2019). TICON: Tidal constants based on gesla sea-level records from globally located tide gauges. *Geoscience Data Journal*, *6*(2), 97–104. https://doi.org/10.1002/gdj3.72

Ponte, R. M., & Ray, R. D. (2002). Atmospheric pressure corrections in geodesy and oceanography: A strategy for handling air tides. *Geophysical Research Letters*, *29*(24), 6-1–6-4. https://doi.org/10.1029/2002GL016340

Pugh, D., & Woodworth, P. (2014). *Sea-level science: Understanding tides, surges, tsunamis and mean sea-level changes*. Cambridge University Press. https://doi.org/10.1017/CBO9781139235778

Rapp, R. H. (1982). Degree variances of the Earth's potential, topography and its isostatic compensation. *Bulletin Geodesique*, *56*(2), 84–94. https://doi.org/10.1007/bf02525594

Ray, R. D. (1998a). Diurnal oscillations in atmospheric pressure at twenty-five small oceanic islands. *Geophysical Research Letters*, *25*(20), 3851–3854. https://doi.org/10.1029/1998gl900039

Ray, R. D. (1998b). Ocean self-attraction and loading in numerical tidal models. *Marine Geodesy*, *21*(3), 181–192. https://doi.org/10.1080/01490419809388134

Ray, R. D. (2013). Precise comparisons of bottom-pressure and altimetric ocean tides. *Journal of Geophysical Research: Oceans*, *118*(9), 4570–4584. https://doi.org/10.1002/jgrc.20336

Ray, R. D., & Egbert, G. D. (2004). The global S_1 tide. *Journal of Physical Oceanography*, *34*(8), 1922–1935. https://doi.org/10.1175/1520-0485(2004)034<1922:tgst>2.0.co;2

Ray, R. D., & Ponte, R. M. (2003). Barometric tides from ECMWF operational analyses. *Annales Geophysicae*, *21*(8), 1897–1910. https://doi.org/10.5194/angeo-21-1897-2003

Ray, R. D., & Poulose, S. (2005). Terdiurnal surface-pressure oscillations over the continental United States. *Monthly Weather Review*, *133*(9), 2526–2534. https://doi.org/10.1175/MWR2988.1

Ray, R. D., Boy, J.-P., Arbic, B. K., Egbert, G. D., Erofeeva, S. Y., Petrov, L., & Shriver, J. F. (2021). The problematic ψ^1 ocean tide. *Geophysical Journal International*, *227*(2), 1181–1192. https://doi.org/10.1093/gji/ggab263

Röske, F. (2005). Global oceanic heat and fresh water forcing datasets based on ERA-40 and ERA-15. *Reports on Earth System Science*, *13*.

Saha, S., Moorthi, S., Wu, X., Wang, J., Nadiga, S., Tripp, P., et al. (2014). The NCEP climate forecast system version 2. *Journal of Climate*, *27*(6), 2185–2208. https://doi.org/10.1175/JCLI-D-12-00823.1

Schindelegger, M., & Dobslaw, H. (2016). A global ground truth view of the lunar air pressure tide L_2. *Journal of Geophysical Research: Atmospheres*, *121*(1), 95–110. https://doi.org/10.1002/2015JD024243

Schindelegger, M., Einšpigel, D., Salstein, D., & Böhm, J. (2016). The global S_1 tide in Earth's nutation. *Surveys in Geophysics*, *37*(3), 643–680. https://doi.org/10.1007/s10712-016-9365-3

Schindelegger, M., Green, J. A. M., Wilmes, S.-B., & Haigh, I. D. (2018). Can we model the effect of observed sea level rise on tides? *Journal of Geophysical Research: Oceans*, *123*(7), 4593–4609. https://doi.org/10.1029/2018JC013959

Schulzweida, U. (2019). CDO user guide [Dataset]. Zenodo. https://doi.org/10.5281/zenodo.3539275

Schulzweida, U. (2022). CDO User Guide [Dataset]. Zenodo. Retrieved from https://doi.org/10.5281/zenodo.7112925

Schureman, P. (1958). *Manual of harmonic analysis and prediction of tides* [revised 1940 edition reprinted 1958 with corrections, reprinted 2001]. United States Government Printing Office.

Sela, J. G. (2010). The derivation of the sigma pressure hybrid coordinate semi-Lagrangian model equations for the GFS. Retrieved from https://repository.library.noaa.gov/view/noaa/6971

Shihora, L., Balidakis, K., Dill, R., Dahle, C., Ghobadi-Far, K., Bonin, J., & Dobslaw, H. (2022). Non-tidal background modeling for satellite gravimetry based on operational ECMWF and ERA5 reanalysis data: AOD1B RL07. *Journal of Geophysical Research: Solid Earth*, *127*(8), e2022JB024360. https://doi.org/10.1029/2022JB024360

Shihora, L., Sulzbach, R., Dobslaw, H., & Thomas, M. (2021). Self-attraction and loading feedback on ocean dynamics in both shallow water equations and primitive equations. *Ocean Modelling*, *169*, 101914. https://doi.org/10.1016/j.ocemod.2021.101914

Simon, B. (2013). *Coastal tides*. Institut Océanographique Éd. Retrieved from https://books.google.de/books?id=oQjsoAEACAAJ

Sulzbach, R., Balidakis, K., Dobslaw, H., & Thomas, M. (2022). TiME22: Periodic disturbances of the terrestrial gravity potential induced by oceanic and atmospheric tides. *GFZ Data Services*. https://doi.org/10.5880/GFZ.1.3.2022.006

Sulzbach, R., Dobslaw, H., & Thomas, M. (2021). High-resolution numerical modeling of barotropic global ocean tides for satellite gravimetry. *Journal of Geophysical Research: Oceans*, *126*(5), e2020JC017097. https://doi.org/10.1029/2020JC017097

Tamura, Y. (1987). A harmonic development of the tide-generating potential. *Bulletin d'Information des Marées Terrestres*, *99*, 6813–6855.

Tapley, B. D., Bettadpur, S., Watkins, M., & Reigber, C. (2004). The gravity recovery and climate experiment: Mission overview and early results. *Geophysical Research Letters*, *31*(9), L09607. https://doi.org/10.1029/2004GL019920

Taszarek, M., Pilguj, N., Allen, J. T., Gensini, V., Brooks, H. E., & Szuster, P. (2021). Comparison of convective parameters derived from ERA5 and MERRA-2 with rawinsonde data over Europe and North America. *Journal of Climate*, *34*(8), 3211–3237. https://doi.org/10.1175/JCLI-D-20-0484.1

Teitelbaum, H., & Vial, F. (1981). Momentum transfer to the thermosphere by atmospheric tides. *Journal of Geophysical Research*, *86*(C10), 9693–9697. https://doi.org/10.1029/JC086iC10p09693

Tierney, C., Wahr, J., Bryan, F., & Zlotnicki, V. (2000). Short-period oceanic circulation: Implications for satellite altimetry. *Geophysical Research Letters*, *27*(9), 1255–1258. https://doi.org/10.1029/1999gl010507

van den Dool, H. M., Saha, S., Schemm, J., & Huang, J. (1997). A temporal interpolation method to obtain hourly atmospheric surface pressure tides in reanalysis 1979–1995. *Journal of Geophysical Research*, *102*(D18), 22013–22024. https://doi.org/10.1029/97JD01571

Vial, F., & Forbes, J. (1994). Monthly simulations of the lunar semi-diurnal tide. *Journal of Atmospheric and Terrestrial Physics*, *56*(12), 1591–1607. https://doi.org/10.1016/0021-9169(94)90089-2

Wang, H., Xiang, L., Jia, L., Jiang, L., Wang, Z., Hu, B., & Gao, P. (2012). Load love numbers and green's functions for elastic Earth models PREM, iasp91, ak135, and modified models with refined crustal structure from Crust 2.0. *Computers & Geosciences*, *49*, 190–199. https://doi.org/10.1016/j.cageo.2012.06.022

Weis, P., Thomas, M., & Sündermann, J. (2008). Broad frequency tidal dynamics simulated by a high-resolution global ocean tide model forced by ephemerides. *Journal of Geophysical Research*, *113*(C10), C10029. https://doi.org/10.1029/2007JC004556

Wessel, P., Luis, J. F., Uieda, L., Scharroo, R., Wobbe, F., Smith, W. H. F., & Tian, D. (2019). The generic mapping tools version 6. *Geochemistry, Geophysics, Geosystems*, *20*(11), 5556–5564. https://doi.org/10.1029/2019gc008515

Wolff, J.-O., Maier-Reimer, E., & Legutke, S. (1997). The Hamburg ocean primitive equation model HOPE. Technical Report 13. https://doi.org/10.2312/WDCC/DKRZ_Report_No13